*Electronic Letters on Computer Vision and Image Analysis 21(1):47-58, 2022*

# Object Detection and Statistical Analysis of Microscopy Image Sequences *

Sasha Hurovitz*, Debora Chan+ Rodrigo Ramele* and Juliana Gambini* ++

* *Depto. de Ingeniería en Informática, Instituto Tecnológico de Buenos Aires, Buenos Aires, Argentina;*
+ *Depto. de Matemática, Universidad Tecnológica Nacional, Regional Buenos Aires, Buenos Aires, Argentina;*
++ *Depto. de Ingeniería en Computación, UNTreF, Pcia. de Buenos Aires, Argentina;*

Received 1st August, 2021; accepted 21st April 2022

**Abstract**

Confocal microscope images are wide useful in medical diagnosis and research. The automatic interpretation of this type of images is very important but it is a challenging endeavor in image processing area, since these images are heavily contaminated with noise, have low contrast and low resolution. This work deals with the problem of analyzing the penetration velocity of a chemotherapy drug in an ocular tumor called retinoblastoma. The primary retinoblastoma cells cultures are exposed to topotecan drug and the penetration evolution is documented by producing sequences of microscopy images. It is possible to quantify the penetration rate of topotecan drug because it produces fluorescence emission by laser excitation which is captured by the camera. In order to estimate the topotecan penetration time in the whole retinoblastoma cell culture, a procedure based on an active contour detection algorithm, a neural network classifier and a statistical model and its validation, is proposed. This new inference model allows to estimate the penetration time. Results show that the penetration mean time strongly depends on tumorsphere size and on chemotherapeutic treatment that the patient has previously received.

*Key Words*: Confocal Microscopy, Retinoblastoma, Active contours, Machine Learning, Segmentation.

## 1 Introduction

Automatic interpretation of microscopy images is a challenge in the area of image processing because they are contaminated with noise, they have low contrast and low resolution. This type of images is wide useful in medicine studies for researching in different diseases and drugs.

Retinoblastoma is the most frequent ocular tumor in childhood, characterized by malignant cells in the retina. One of the treatments used in retinoblastoma fighting is topotecan drug [18, 23]. The objective of this work is the automatic interpretation of microscopy image sequences and to propose a series of standard steps for analyzing this type of images by using active contours and machine learning techniques for image segmentation and classification, respectively. The advantage of topotecan drug is that its penetration can be quantified through its fluorescence emission by laser excitation [18]. The images were taken at Prof. Dr. Juan Pedro Garrahan

Correspondence to: <rramele@itba.edu.ar>

Recommended for acceptance by Angel D. Sappa
https://doi.org/10.5565/rev/elcvia.1482
ELCVIA ISSN:1577-5097
Published by Computer Vision Center / Universitat Autònoma de Barcelona, Barcelona, Spain

Hospital, Buenos Aires by expert professionals. The microscope used is Olympus Fluoview FV1000 confocal laser scanning microscope (Olympus, Tokyio, Japan) with imaging software (Olympus Fluoview FV10-ASW v1.7c) and equipped with a UPlanSApo 20X / 0.75 NA objective, for more information see [2].

Several authors have studied retinal diseases by means of medical images analysis and statistical modeling. In [19] a study of tumor classification using 395 fundus images is presented. In this article, the authors construct a probabilistic framework for retinal diseases diagnosis, with information that they obtain by capturing historical knowledge of retinal pathologies, from a bank of fundus image. Other authors [3, 21] have explored automatic techniques of pathology tracking by means of image analysis. In [17] a work focused on retinoblastoma detection by using image processing, is exposed. The authors perform a review of image segmentation and classification methods, all of them applied to retinal images. An additional method is presented in [24] where a vessel segmentation procedure with application to retinal disease study, using active contours, is introduced. Although all these works dealt on experiments performed on retinal images, as far as we are aware of, until now, none had been performed on tumor cells microscope images. In [4], a prediction of retinoblastoma presence using convolutional neural networks (CNN), is presented. In [22] the authors contribute to the understanding of retinal tumor cells by producing tridimensional retinoblastoma cultures as vitreous seeds models for live-cell imaging of chemotherapy penetration. In [2] an assessment of topotecan penetration time in tumorspheres was carried out by means of a statistical model, but the results were ambiguous. Further improving on those ideas, in this paper we focus on image sequence analysis and preprocessing techniques combined with data analysis, in order to characterize the dynamics of topotecan penetration in tumor cell clusters. In this article, the penetration percentage for each given time is computed more accurately using image segmentation techniques based on morphological geodesic active contours and a machine learning classification.

The images utilized in this study, derive from an experiment from which its biological procedure is explained in [22]. The microscopy images of these cell cultures belong to two patients, each one of a different kind: **Patient 1**, the patient was enucleated in the first line of treatment without having previously received chemotherapy. **Patient 2**, the patient had received chemotherapy prior to the enucleation of the affected eye. The acquisition of primary cultures from tumor cells is an important challenge due to stringent growth and maintenance conditions. The cell cultures used in this work are unique in Argentina [22].

According to [22], cell cultures are exposed to 1 microliter of a 10 $\mu$g/ml solution of topotecan and observed in light gray microscope photos. Finally, an expert takes pictures of the evolution of the drug at regular time intervals. The penetration time of the drug in the tumorsphere is expected to be predicted according to the fluorescence evolution over time by measuring it using image segmentation, statistical inference and machine learning methods. A better understanding of the Topotecan penetration dynamics in Retinoblastoma could help to devise more precise dosage as well as timing constraints of the administering procedure.

These cell cultures, to which we refer to as tumorspheres, are classified by visual inspection, according to their size, into three categories: small, medium and large. Figure 1 shows an example of a sequence of microscopy images corresponding to a large size tumorsphere from Patient 1. It can be observed that gray levels of pixels become brighter as time passes by. As topotecan penetrates the cell, it takes on brighter gray levels.

The objectives of this work are: In first place, the automatic interpretation of the image sequences and then, build a model to automatically estimate the time that topotecan consumes in penetrating the whole tumorsphere. The tumorsphere is considered to have been totally penetrated when it has a homogeneous color in the central region. Compare the penetration rate of topotecan between types of tumorspheres from Patient 1 and Patient 2. Compare the penetration rate of topotecan between different sizes of tumorspheres, derived from the same patient.

This article unfolds as follows. In Section 2, the image processing techniques to segment the microscopy image and the neural network based classification method, are described. Section 3 shows the model to estimate the topotecan penetration time. Section 4 presents the results of applying the image segmentation and classification methods and the validation of the statistical analysis. Lastly, in Section 5, final remarks are exhibited.

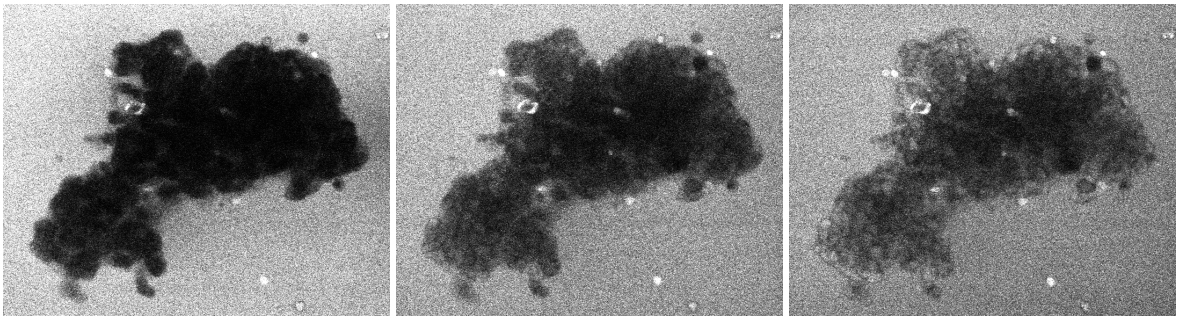

(a) Time 0 s (b) Time 30 s (c) Time 60 s

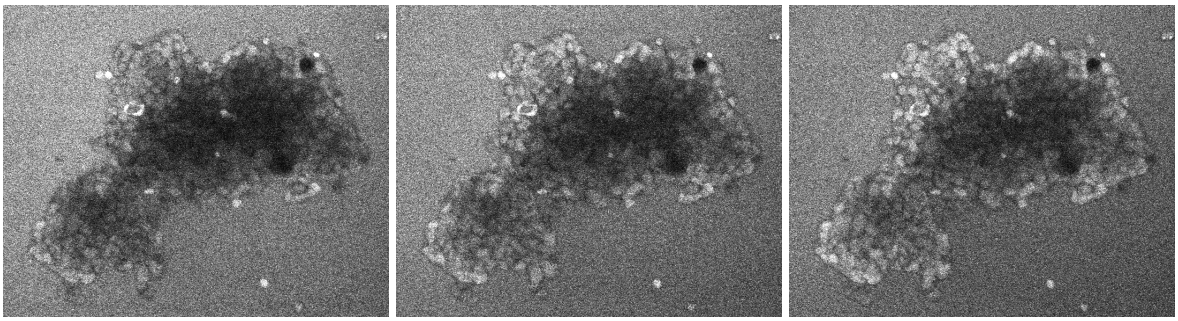

(d) Time 90 s (e) Time 120 s (f) Time 150 s

Figure 1: Sequence of microscopy images taken at 30 seconds intervals, corresponding to a large size tumorsphere from Patient 1.

## 2 Object Detection and Pixel Classification

The microscopy images are contaminated with noise which can be observed as a granulation. Figure 1 shows an example of an image sequence where none image improvement technique was applied. Noise confuses automatic methods of image interpretation and it is necessary to eliminate it before starting the analysis. A method of noise removal with edge preservation called Bilateral Filter [20] is applied, because it balances noise reduction and edge preservation against low computational cost [9].

As the underlying objective is to evaluate the topotecan penetration dynamics in the tumorsphere, it is relevant to identify with high precision the pixels that belong to the cell. Hence, this implies recognizing as accurate as possible the tumorsphere contour. Then, the pixels inside the contour are considered. There are many different approaches for object segmentation in medical images. One of them is manual delimitation but it is time-consuming, tedious and the results can be subjective and non-repeatable. On the other hand, fully automatic methods require a prior object shape knowledge, which is not usually available in medical images. Halfway of these opposite ends, semiautomatic methods provide a balance between good results and low user intervention. The image segmentation methods based on active contours belong to the latter class [16, 15]. These type of algorithms begin with an initial curve provided by the user, which evolves to fit the edge of the object of interest. Geodesic active contours is an example of this type of algorithms [1, 8], based on the computation of the minimal length curve. This method has the property of being more accurate at contour fitting than other methods based on curve evolution, though it carries a higher computational cost. In [14] a formal approach for stable and fast contour evolution is provided by using morphological operators combined with geodesic active contours, called Morphological Geodesic Active Contour (MGAC) method. This implementation is easier since it does not require the use of sophisticated numerical algorithms and provide almost the same solution that geodesic active contours and, according to authors, it offers advantages in terms

of speed and stability.

In this case, as the topotecan drug spreads across the culture, precision in fitting the object contour is essential. In [2], an active contours method based on pixels interchange between two lists of neighbor pixels was used for tumorsphere segmentation. This method is very fast but the contour fitting was not accurate in some images and therefore ambiguous results were obtained. The lack of good results was found to be the high contrast inside the tumorsphere. For this reason, the MGAC algorithm being more stable, is a good alternative solution.

Figure 2 shows the result of applying the MGAC method to the first image of a sequence of a retinoblastoma cluster. Figure 2a shows the initial curve, a polygonal given by the user in a roughly way. Figure 2b shows the result of applying the MGAC method, and the segmented results is depicted on Figure 2c. It can be observed the precision of the contour finding method.

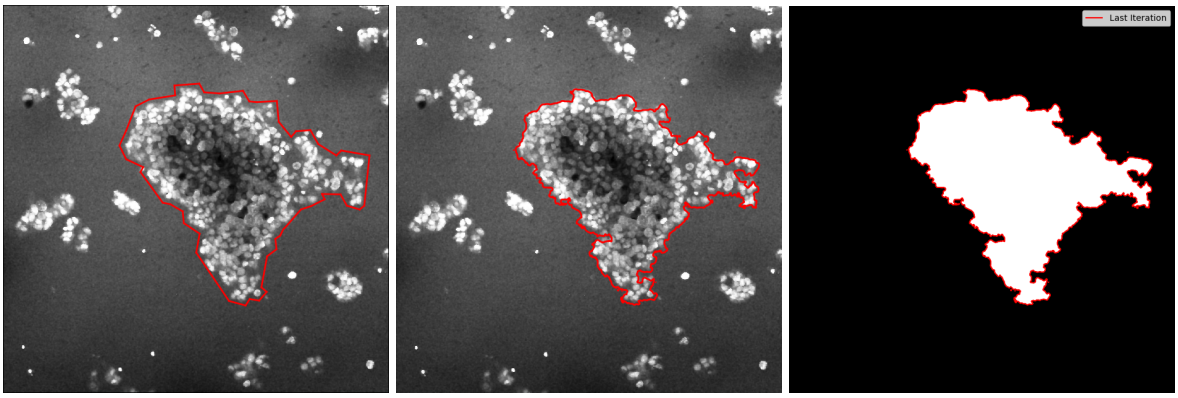


(a) Initial curve (b) Final Curve (c) Segmented Result

Figure 2: Result of applying the MGAC method to a retinoblastoma cell cluster image.

Once the pixels belonging to the tumorsphere have been found, it is necessary to classify them into two levels, assigning to each pixel the $YES$ or the $NO$ labels, where the first indicates topotecan presence. Hence, from the classification, the percentage of topotecan penetration into the tumorsphere can be calculated.

Supervised learning classification methods are based on a labeled training set, that provides classes information. In this way, it is possible to classify a testing set by the labeled information acquired from a previous training set. Convolutional neural networks (CNN) belong to this kind of methods [13]. However, in this case, the true classification of the pixels is unknown, there is no labeled training set, and it cannot even be obtained by an expert. In order to properly classify the pixels without prior information, we utilize the method presented in [11]. In contrast, this algorithm is an unsupervised image classification method based on convolutional neural networks. It is a combination between label prediction and network parameter learning. The authors demonstrated that this method is more efficient that $k$-means [12] and graph-based [5] classification methods. Once the classification is performed in the whole sequence, it is possible to compute the percentage of white pixels, and in consequence, the percentage of topotecan cell penetration. Figure 3 shows the pipeline of the whole process.

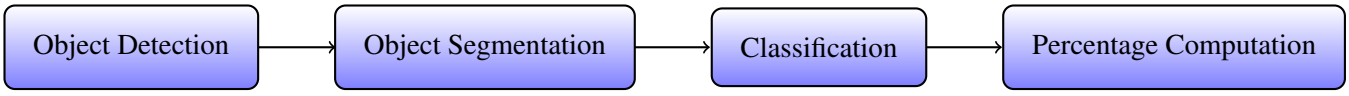


Figure 3: Scheme of the proposed process.

## 3 Penetration time estimation with qualitative predictors

In this section, we compute a linear model with qualitative predictors with three levels, to estimate the time it takes for the topotecan to reach the total penetration. In order to build a model for topotecan penetration time estimation by comparing medium and small sizes with large size, the following model is used,

$$T^p = \beta_0^p + \beta_1^p X_1^p + \beta_2^p X_2^p + \epsilon \tag{1}$$

where $p = \{1, 2\}$ correspond to Patient 1 and Patient 2, respectively. The dummy variables are

$$X_1^p = \begin{cases} 1 & if\ Size = M \\ 0 & if\ Size \neq M \end{cases} \tag{2}$$

and

$$X_2^p = \begin{cases} 1 & if\ Size = S \\ 0 & if\ Size \neq S \end{cases} \tag{3}$$

where $M$ and $S$ are medium and small sizes, respectively.

The models are validated following the recommendations by [10]. We compute $R^2$ error and Adjusted $R^2$ error (see [7]), which provide a measure of lack of fit of the model. They range between 0 and 1, where 1 indicates a perfect fit. And the $t$- Student test, with a significance level $\eta = 0.05$:

$$\begin{aligned} H_0 &: \quad \beta_i = 0,\ i = 0, 1, 2 \\ H_a &: \quad \beta_i \neq 0\ i = 0, 1, 2 \end{aligned}$$

The Fisher test (see [6]) with a significance level $\eta = 0.05$:

$$\begin{aligned} H_0 &: \quad \beta_0 = \beta_1 = \beta_2 = 0 \\ H_a &: \quad \exists \beta_i \neq 0\ i \in \{0, 1, 2\} \end{aligned}$$

In Section 4 the results of validation are presented.

## 4 Results

Table 1 shows the average number of pixels that small, medium and large size tumorspheres possess, respectively.

Table 1: Pixel average number for each tumorsphere size.

| | S | M | L |
|---|---|---|---|
| Number of Pixels | 110619 | 162062 | 339129 |

Figure 4 shows the result of applying the proposed method to the sequence of Figure 1, using two clusters. It can be observed that the zones that inside/outside regions of the tumorsphere are clearly identified and that the bright zone (topotecan) increases as time passes.

The percentage of topotecan penetration inside the cell is computed by measuring the percentage of white pixels inside the cell. This is presented in Table 2 showing the results of applying this idea to the image sequence of Figure 1.

Table 3 shows the mean penetration rate for each type of cell at 60 seconds. It can be observed that as cell size increases, average penetration rate decreases. In addition, tumorspheres from Patient 2 have a lower average penetration rate.

Figure 5 shows the variation of topotecan penetration rate, depending on the exposure time in conjunction with a polynomial approximation curve for each size of tumorsphere. Figures 5a and 5b correspond to Patient 1

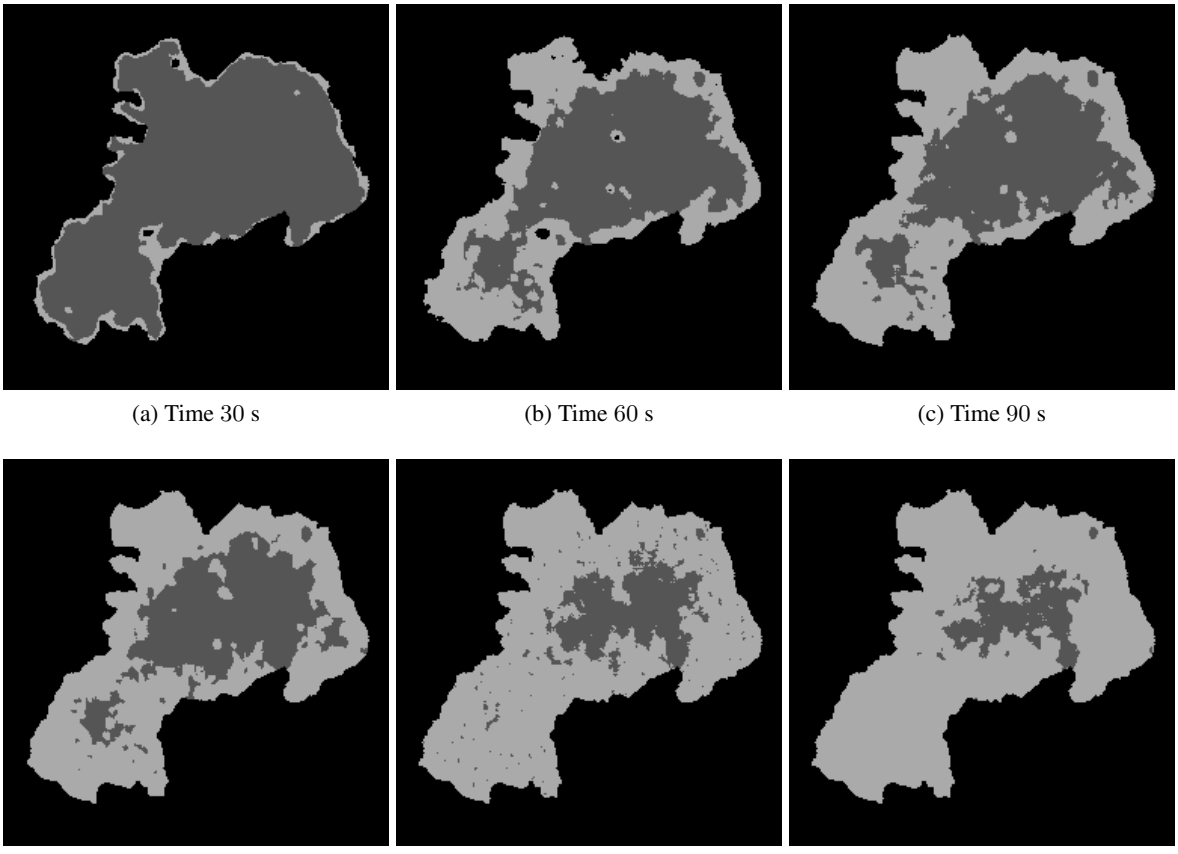

(a) Time 30 s (b) Time 60 s (c) Time 90 s

(d) Time 120 s (e) Time 150 s (f) Time 180 s

Figure 4: Results of applying the unsupervised image classification method to the images of Figure 1.

and Patient 2, respectively. All regression curves are increasing functions, indicating the penetration rate increases with the passage of time.

Figure 6 shows the variation of topotecan penetration rate, depending on the exposure time in a boxplot graph. Figures 6a and 6b correspond to Patient 1 and Patient 2, respectively. It can be observed that as tumorsphere size increases, the width of the boxplot increases, indicating an increment in the penetration time.

Tables 4 and 5 show the obtained linear model results for the Patient 1 model. They exhibit the coefficient estimates, its standard error, the results of applying the $t$ test, the $R^2$ error, the adjusted $R^2$ error and the results of applying the Fisher test.

The negative sign of coefficients $\hat{\beta}_1^1$ and $\hat{\beta}_2^1$ indicates that as the size of the tumorsphere is smaller, the penetration time decreases. It can be observed, in the $p$-value column, that the null hypothesis of $t$-test is rejected with a significance level $\eta = 0.05$. It shows that the estimated coefficients $\hat{\beta}_0^1$, $\hat{\beta}_1^1$ and $\hat{\beta}_2^1$ are significantly different of zero. Fisher test $p$-value $= 4.269e - 07$ from Table 5 shows that the null hypothesis of Fisher test is rejected with a significance level $\eta = 0.05$. $R^2 > 0.5$ and Adjusted $R^2 > 0.5$ indicate an admissible error.

Table 6 shows the topotecan complete penetration time estimates (in seconds) for Patient 1, following the model from Eq. 1.

Tables 7 and 8 show the linear model results for Patient 2 model. The negative sign of coefficients $\hat{\beta}_1^2$ and $\hat{\beta}_2^2$ indicates that as the size of the tumorsphere is smaller, the penetration time decreases. It can be observed in the $p$-values column that the null hypothesis of $t$-test is rejected with a significance level $\eta = 0.05$. It shows that the estimated coefficients $\hat{\beta}_0^2$, $\hat{\beta}_1^2$ and $\hat{\beta}_2^2$ are significantly different of zero. Fisher test $p$-value from Table 8 shows

Table 2: Topotecan penetration rate for the segmented image sequence of Figure 4.

| Image | Time (s) | Percentage |
|---|---|---|
| 1 | 0 | 0% |
| 2 | 30 | $10,27\%$ |
| 3 | 60 | $45,94\%$ |
| 4 | 90 | $54,87\%$ |
| 5 | 120 | $63,70\%$ |
| 6 | 150 | $81,14\%$ |
| 7 | 180 | $87,90\%$ |

Table 3: Average penetration rate at 60s.

| | S | M | L |
|---|---|---|---|
| Patient 1 | 67.82% | 59.96% | 36.01% |
| Patient 2 | 66.62% | 15.44% | 12.83% |

that the null hypothesis of Fisher test is rejected and $R^2 > 0.5$ and Adjusted $R^2 > 0.5$ indicate an admissible error. Table 9 shows the topotecan complete penetration time estimates (in seconds) for Patient 2, following the model from Eq. 1.

It can be observed that $\hat{\beta}_i^2 >> \hat{\beta}_i^1 \; \forall \; i = \{0, 1, 2\}$ which shows that penetration time in tumorspheres from Patient 1 is lower than in tumorspheres from Patient 2.

We have shown that the data satisfy the Gaussian distribution but we did not include the results for space reasons.

## 5 Conclusions and Future work

Microscopy images are noisy and have low contrast. Hence, their automatic analysis is a challenging endeavor. In this work, we perform a study on microscopy image sequences with advanced image analysis procedures which allows automatically observe the evolution of the topotecan within tumor cells.

Based on visual expert observation, we verified that the active contour method MGAC is very accurate in finding the tumorspheres contour. The machine learning pixel classification method has a solid theory that supports it and produces very reliable results. In order to estimate the penetration time of topotecan, we use a qualitative predictors multiple linear model. Computed statistics show that the model fits the data with precision, providing good estimates. Additionally, results show that topotecan penetration rate in tumorspheres from Patient 1 is faster than in tumorspheres from Patient 2, 27% faster for tumorspheres of large size, 32% faster for medium size and 43% faster for small size.

Our findings confirm that the time of topotecan penetration into the retinoblastoma cell is greatly affected by the size of the tumorspheres and by the chemotherapeutic treatment that the patient has previously received. These automatic procedures could potentially help to understand chemotherapeutic dosage and timing constraints.

This work has several limitations. First, tumorspheres are tridimensional structures that are flattened in order to be used on the microscopy. Additionally, the parameters of the topocan penetration dynamics is different for 2 patients, and this may hinder the use of a generalized model for clinical use. Although the acquisition of this type of images from cell cultures is a very daunting and time consuming procedure, the size of the test dataset (two test persons) allows a limited proof-of-concept validation that requires further experimentation in order to generalize the results and their applicability. Due to the complexities of the generation of cell cultures, increasing the size of the dataset by acquiring more images is not a valid option. Hence, future work points

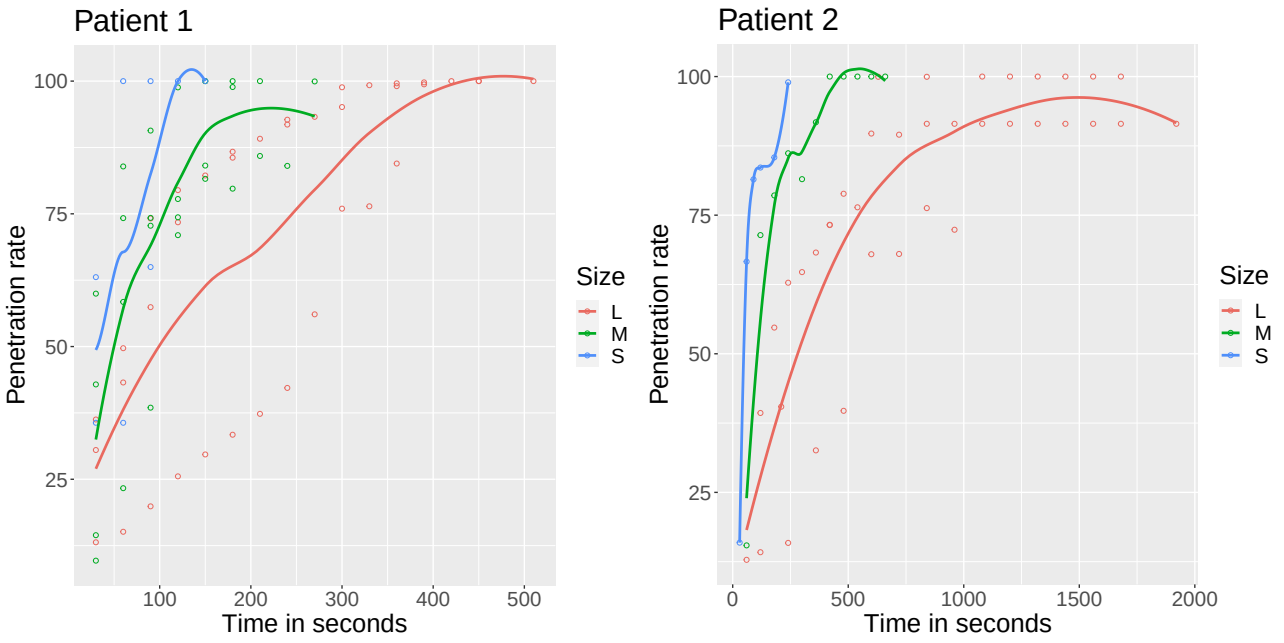


(a) Patient1

(b) Patient2

Figure 5: Penetration rate vs. time, depending on tumorspheres size for Patient 1 ( 5a) and Patient 2 ( 5b). The curves indicate polynomial approximation for each dataset.

Table 4: Coefficient Estimates Patient 1.

| | Estimate | Std. Error | $t$ value | $p$-value |
|---|---|---|---|---|
| $\hat{\beta}_0^1$ | 357.86 | 18.90 | 18.934 | 1.59e-15 |
| $\hat{\beta}_1^1$ | -189.11 | 31.34 | -6.034 | 3.74e-06 |
| $\hat{\beta}_2^1$ | -252.86 | 40.09 | -6.307 | 1.96e-06 |

towards the generation of synthetic data that could capture the specific characteristic of these fluorescence microscopic images by using Generative approaches for data augmentation like Variational Autoencoders (VAE) or Generative Adversarial Networks (GAN).

Table 5: Patient 1 model validation.

| $R^2$ | Adjusted $R^2$ | $\mathcal{F}$-statistic | $p$-value |
|---|---|---|---|
| 0.7207 | 0.6964 | 29.67 | 4.269e-07 |

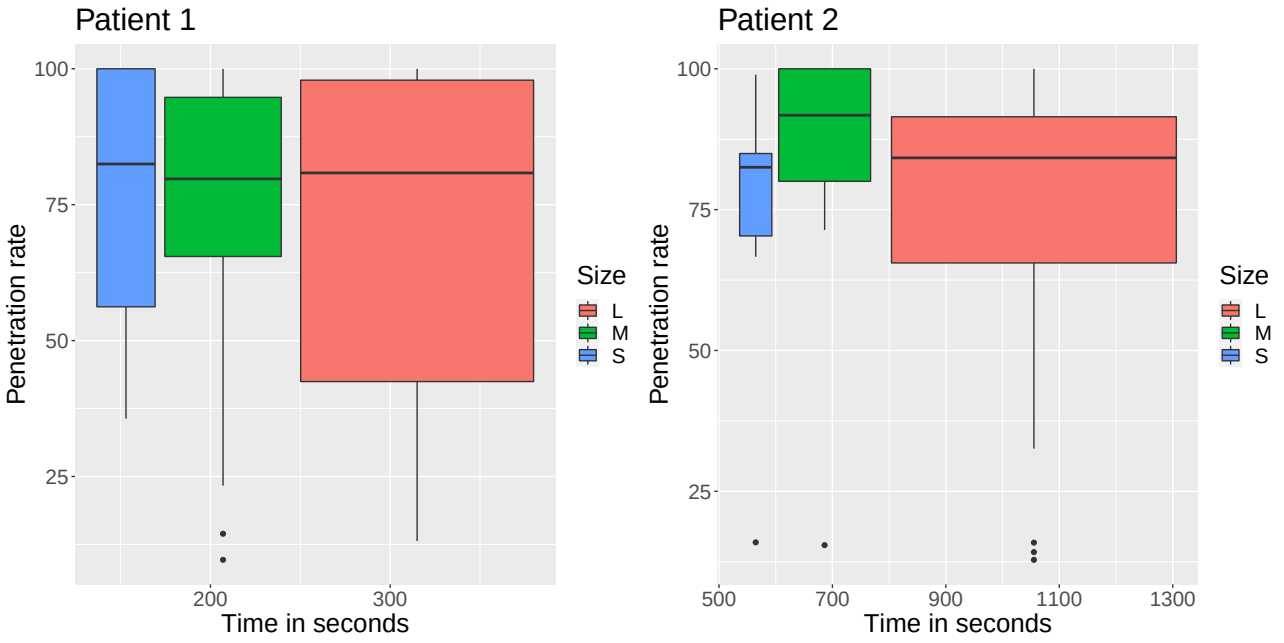


(a) Patient1

(b) Patient2

Figure 6: Penetration rate vs. time in a boxplot graph, depending on tumorspheres size, for Patient 1 ( 6a) and Patient 2 ( 6b).

Table 6: Penetration time estimates, following Eq. 1, Patient 1.

| Size | $L$ | $M$ | $S$ |
|---|---|---|---|
| $\hat{T}$ | 357.86 | 168.75 | 105 |

Table 7: Coefficient Estimates Patient 2.

| | Estimate | Std. Error | $t$ value | $p$- value |
|---|---|---|---|---|
| $\hat{\beta}_0^2$ | 1279.41 | 75.01 | 17.056 | 8.82e-14 |
| $\hat{\beta}_1^2$ | -769.41 | 146.86 | -5.239 | 3.42e-05 |
| $\hat{\beta}_2^2$ | -1039.41 | 318.24 | -3.266 | 0.00369 |

Table 8: Patient 2 model validation.

| $R^2$ | Adjusted$R^2$ | $\mathcal{F}$-statistic | $p$-value |
|---|---|---|---|
| 0.6216 | 0.5855 | 17.25 | 3.704e-05 |

Table 9: Penetration time estimates, following Eq. 1, Patient 2.

| Size | $L$ | $M$ | $S$ |
|---|---|---|---|
| $\hat{T}$ | 1279.41 | 519 | 240 |

## Conflict of interest

The authors declare that they have no conflict of interest.

## References


[1] V. CASELLES, R. KIMMEL, and G. SAPIRO, Geodesic active contours, *International Journal of Computer Vision* **22** no. 1 (1997), 61–79. doi:10.1023/A:1007979827043.

[2] D. CHAN, U. WINTER, P. SCHAIQUEVICH, R. RAMELE, and J. GAMBINI, Time estimation of topotecan penetration in retinoblastoma cells through image sequences analysis, in *VIII Congreso Latinoamericano de Ingeniería Biomédica. CLAIB 2019*, 2019. doi:10.1109/SIBGRAPI.2008.36.

[3] A. COSCI, A. TAKAHAMA, W. CORRER, R. SOUZA AZEVEDO, K. FERNANDES DA COSTA FONTES, and C. KURACHI, Automated algorithm for actinic cheilitis diagnosis by wide-field fluorescence imaging, *Journal of Medical Imaging* **3** no. 4 (2016), 1–6. doi:10.1117/1.JMI.3.4.044004.

[4] C. A. DURAI, T. JEBASEELI, S. ALELYANI, and A. MUBHARAKALI, Early prediction and diagnosis of retinoblastoma using deep learning techniques, *CoRR* **abs/2103.07622** (2021), 1–17. Available at `https://arxiv.org/abs/2103.07622`.

[5] P. F. FELZENSZWALB and D. P. HUTTENLOCHER, Efficient graph-based image segmentation, *International Journal of Computer Vision* **59** no. 2 (2004), 167–181. doi:10.1023/B:VISI.0000022288.19776.77.

[6] R. FISHER, The goodness of fit of regression formulae, and the distribution of regression coefficients, *Journal of the Royal Statistical Society* **85** no. 4 (1922), 597–612. doi:10.2307/2341124.

[7] D. A. FREEDMAN, *Statistical Models: Theory and Practice*, Cambridge University Press, 2009.

[8] R. GOLDENBERG, R. KIMMEL, E. RIVLIN, and M. RUDZSKY, Fast geodesic active contours, *IEEE Trans. Image Processing* **10** no. 10 (2001), 1467–1475. doi:10.1109/83.951533.

[9] S. A. HAIDER, A. CAMERON, D. SIVA, P.AND LUI, A. SHAFIEE, M. J.AND BOROOMAND, N. HAIDER, and A. WONG, Fluorescence microscopy image noise reduction using a stochastically-connected random field model, *Nature Scientific report* **6** (2016), 20640. doi:10.1038/srep20640.

[10] G. JAMES, D. WITTEN, T. HASTIE, and R. TIBSHIRANI, *An Introduction to Statistical Learning: with Applications in R*, Springer, 2013. Available at `https://faculty.marshall.usc.edu/gareth-james/ISL/`.

[11] A. KANEZAKI, Unsupervised image segmentation by backpropagation, in *IEEE International Conference on Acoustics, Speech and Signal Processing, ICASSP*, 2018, pp. 1543–1547. doi:10.1109/ICASSP.2018.8462533.

[12] S. P. LLOYD, Least squares quantization in pcm, *IEEE Transactions on Information Theory.* **28** no. 2 (1982), 129–137. doi:10.1109/TIT.1982.1056489.

[13] J. LONG, E. SHELHAMER, and T. DARRELL, Fully convolutional networks for semantic segmentation, in *IEEE Conference on Computer Vision and Pattern Recognition (CVPR)*, 2015, pp. 3431–3440. doi:10.1109/TPAMI.2016.2572683.

[14] P. MÁRQUEZ-NEILA, L. BAUMELA, and L. ALVAREZ, A morphological approach to curvature-based evolution of curves and surfaces, *IEEE Transactions on Pattern Analysis and Machine Intelligence* **36** no. 1 (2014), 2–17. doi:10.1109/TPAMI.2013.106.

[15] S. OSHER and N. PARAGIOS, *Geometric Level Set Methods in Imaging, Vision, and Graphics*, Springer-Verlag, 2003.

[16] S. OSHER and J. SETHIAN, Fronts propagating with curvature dependent speed: Algorithms based on Hamilton-Jacobi formulations, *Journal of Computational Physics* **79** (1988), 12–49. doi:10.1016/0021-9991(88)90002-2.

[17] S. SADHANA and D. MALLIKA, A review of retina blood vessel detection using image segmentation techniques, *International Journal for Innovative Research in Science & Technology* **3** (2017), 247–253. doi:10.3390/mi12121478.

[18] P. SCHAIQUEVICH, A. CECILIANO, N. MILLAN, P. TAICH, F. VILLASANTE, A. C. FANDINO, J. DOMINGUEZ, and G. L. CHANTADA, Intra-arterial chemotherapy is more effective than sequential periocular and intravenous chemotherapy as salvage treatment for relapsed retinoblastoma, *Pediatric blood & cancer* (2013), 766–770. doi:10.1002/pbc.24356.

[19] K. W. TOBIN, M. ABDELRAHMAN, E. CHAUM, V. P. GOVINDASAMY, and T. P. KARNOWSKI, A probabilistic framework for content-based diagnosis of retinal disease, in *IEEE Engineering in Medicine and Biology Society*, 2007, pp. 6743–6746. doi:10.1109/IEMBS.2007.4353909.

[20] C. TOMASI and R. MANDUCHI, Bilateral filtering for gray and color images, in *Sixth International Conference on Computer Vision (IEEE Cat. No.98CH36271)*, 1998, pp. 839–846. doi:10.1109/ICCV.1998.710815.

[21] W. WELGE, A. DEMARCO, J. WATSON, P. RICE, J. BARTON, and J. KUPINSKI, Diagnostic potential of multimodal imaging of ovarian tissue using optical coherence tomography and second-harmonic generation microscopy, *Journal of Medical Imaging* **1** no. 2 (2014), 1–8. doi:10.1117/1.JMI.1.2.025501.

[22] U. WINTER, R. ASCHERO, F. FUENTES, F. BUONTEMPO, S. ZUGBI, M. SGROI, C. SAMPOR, D. ABRAMSON, A. CARCABOSO, and P. SCHAIQUEVICH, Tridimensional retinoblastoma cultures as vitreous seeds models for live-cell imaging of chemotherapy penetration, *International Journal of Molecular Sciences* **20** (2019), 1077. doi:10.3390/ijms20051077.

[23] U. WINTER, M. NICOLAS, M. SGROI, C. SAMPOR, A. TORBIDONI, A. FANDI NO, G. CHANTADA, F. MUNIER, and P. SCHAIQUEVICH, Assessment of retinoblastoma rna reflux after intravitreal injection of melphalan, *British Journal Of Ophthalmology* **3** (2018), 415–418. doi:10.1136/bjophthalmol-2017-310574.

[24] Y. ZHAO, L. RADA, K. CHEN, S. P. HARDING, and Y. ZHENG, Automated vessel segmentation using infinite perimeter active contour model with hybrid region information with application to retinal images, *IEEE Transactions on Medical Imaging* **34** no. 9 (2015), 1797–1807. doi:10.1109/TMI.2015.2409024], url = https://doi.org/10.1109/TMI.2015.2409024,.